The influence of surface ply fibre angle on the compressive strength of composite laminates containing delamination

A. T. Rhead
a.t.rhead@bath.ac.uk

R. Butler
r.butler@bath.ac.uk

W. Liu

N. Baker

Department of Mechanical Engineering
University of Bath
Bath, UK

ABSTRACT

A combination of uniaxial compression tests and Strip Model and Finite Element analyses of laminates artificially delaminated to create circular ($\pm\theta$) sublaminates is used to assess the influence of fibre angle on the compressive strength of composite laminates.

Sublaminates with $0° < \theta < 40°$ are found to fail by sublaminate-buckling-driven delamination propagation and provide poor tolerance of delamination. This is a consequence of their relatively high axial stiffnesses, low sublaminate buckling strains, Poisson's ratio induced compressive transverse strains and extension-twist coupling which produces unexpected sublaminate buckling mode shapes. Sublaminates with $40° < \theta < 60°$ are most tolerant to delamination; axial and transverse stiffnesses are minimal, formation of sublaminate buckles is resisted, high laminate buckling strains reduce interaction between laminate and sublaminate buckling mode shapes and extension-twist coupling is minimal. Sublaminates with $60° < \theta < 90°$ are shown to produce varied tolerance of delamination. Sublaminate buckling is generally prevented owing to transverse tensile strains induced by mismatches between laminate and sublaminate Poisson's ratios but may occur in laminates with low Poisson's ratios.

Paper No. 3886. Manuscript received 13 July 2012, revised version received 4 October 2012, accepted 5 October 2012.

NOMENCLATURE

A_{nn} axial stiffness in either the longitudinal (n = 1) or transverse (n = 2) directions
(A) matrix coupling in-plane loads to in-plane strains
(B) matrix coupling in-plane loads/strains to out-of-plane curvatures/moments
(D) matrix coupling out-of-plane moments to out-of-plane curvatures
E_{11} elastic modulus of layer in the fibre direction
E_{22} elastic modulus of layer perpendicular to the fibre direction
G_{12} shear modulus
G strain energy release rate (SERR)
G_{IC} critcal SERR required to cause Mode I failure of the matrix
{**N**} in-plane load vector
{**M**} out-of-plane moment vector
x in-plane co-ordinate in the longitudinal direction
y in-plane co-ordinate in the transverse direction
z out-of-plane co-ordinate
{**ε**} in-plane strain vector
ε^C sublaminate buckling strain
ε_{th} threshold strain below which propagation will not occur
{**κ**} out-of-plane curvature vector
v_{12} major Poisson's ratio of layer
$v_{\pm\theta}$ sublaminate Poisson's ratio
v_L laminate Poisson's ratio

1.0 INTRODUCTION

Aerospace regulations specify that composite laminates must tolerate Barely Visible Impact Damage (BVID) without failure, typically reducing allowable strains to around 4,500 μstrain (or less in hot wet conditions). In some applications this gives strengths that are less than 50% of the equivalent values for aluminium; a consequence of composite laminates with BVID subject to compression being known to fail at loads significantly below those of pristine laminates. Often this is due to the propagation of delaminations driven by localised sublaminate buckling.

Current commercial aircraft employ laminates comprising 0°, ±45° and 90° plies, for which Compression After Impact (CAI) strength has been determined using extensive experimental testing. However, new fibre steering technologies[1,4] which employ the full gamut of ±θ° plies are giving rise to optimised laminates with tailored stiffness and lower mass. The use of non-standard ply angles in these techniques produces varied CAI problems and novel behaviours that are not well understood.

The method usually adopted for modelling delamination propagation following sublaminate buckling is non-linear Finite Element Analysis (FEA) using cohesive elements or virtual crack closure techniques[5-9]. However, such methods are complex and generally require significant computational effort. Hence their use in understanding the mechanisms affecting damage tolerance is limited. Thus, the development of simplified methods to capture such mechanisms is required in order to improve the design of laminates for damage tolerance.

In this paper the resistance of laminates with ±θ° outer plies to delamination propagation is studied by placing laminates with a single, circular artificial delamination creating a (±θ) sublaminate, under axially compressive end displacement. Here, delamination is fixed, however,

https://doi.org/10.1017/S000192400000765X Published online by Cambridge University Press

for laminates based on the ply angles 0°, ±45° and 90°, similar studies have explored the effect of altering the through-thickness position of the delamination[5,10], the stacking sequence of the sublaminate[5], the shape of delamination[11] and the effect of multiple delaminations[11-13].

In earlier work[14], the authors extended the principles of Strain Energy Release Rate (SERR) considered by others[15-17] for one-dimensional propagation of an isotropic strut containing a delamination to the case of a two-dimensional, anisotropic plate. In this paper, recently derived[5] extensions to the extremely efficient Strip Model are used to understand factors affecting the propagation of a single near surface, circular delamination below a (±θ) sublaminate. A combination of uniaxial compression tests and Strip Model and Finite Element analyses are used to assess the effect that varying θ from 0 to 90° has on the strain at which sublaminate buckling-driven delamination propagation occurs. Previously unseen effects related to mis-matches in Poisson's ratio between the full laminate and sublaminate and to extension-twist coupling in the sublaminate were noted in the experiments and are investigated herein. Interaction of overall laminate deformation and buckling with local sublaminate buckling modes was observed to have a detrimental effect on CAI[10,18].

2.0 ANALYSIS

2.1 The Strip Model

In the following, the delaminated sublaminate will be referred to as the 'sublaminate' and the complete laminate inclusive of the sublaminate as the 'laminate'. Subscripts ±θ and *L* will be used for terms relating to the sublaminate and laminate respectively. Compressive strain is taken to be positive.

The Strip Model[5,14] predicts critical threshold values of applied strain below which sublaminate buckling-driven propagation of a delamination will not occur. The delamination considered is circular and creates a two layer sublaminate with stacking sequence (±θ) on one side of the laminate. A thin-film assumption is made which enforces zero curvature in the parent laminate. The Strip Model is comprised of two parts; the first is the calculation of the local buckling strain ε^C using the infinite strip program VICONOPT[19].

For a general laminate the loads {**N**} and moments {**M**} acting on the laminate are linked to the resulting strains {**ε**} and curvatures {**κ**} by the in-plane (**A**), bending (**D**) and coupling (**B**) stiffness matrices,

$$\begin{Bmatrix} N_x \\ N_y \\ N_{xy} \\ M_x \\ M_y \\ M_{xy} \end{Bmatrix}_L = \begin{bmatrix} A_{11} & A_{12} & A_{13} & B_{11} & B_{12} & B_{13} \\ A_{21} & A_{22} & A_{23} & B_{21} & B_{22} & B_{23} \\ A_{31} & A_{32} & A_{33} & B_{31} & B_{32} & B_{33} \\ B_{11} & B_{12} & B_{13} & D_{11} & D_{12} & D_{13} \\ B_{21} & B_{22} & B_{23} & D_{21} & D_{22} & D_{23} \\ B_{31} & B_{32} & B_{33} & D_{31} & D_{32} & D_{33} \end{bmatrix}_L \begin{Bmatrix} \varepsilon_x \\ \varepsilon_y \\ \varepsilon_{xy} \\ \kappa_x \\ \kappa_y \\ \kappa_{xy} \end{Bmatrix}_L \quad \ldots (1)$$

However, as this paper only considers laminates subject to uniaxial compressive strain in the (longitudinal) 0° direction; the principal loading direction for many aerospace components, only N_x is non-zero in the load/moment vector in Equation (1). Following conventional design

https://doi.org/10.1017/S000192400000765X Published online by Cambridge University Press

principles, which seek to avoid undesirable coupling effects such as extension twist and extension bending, the overall laminate is assumed to be balanced and symmetric. Balanced implies each $+\theta°$ ply is balanced by a $-\theta°$ ply at a different location in the stacking sequence. This prevents the laminate shearing in-plane when a compressive strain is applied and hence terms A_{13} and A_{23} (and A_{31} and A_{32} owing to the orthotropic nature of the plies and rotational symmetry of the laminate) which couple in-plane loading to in-plane shearing are equal to zero. The enforcement of symmetry about the mid-plane of the laminate ensures all in-plane to out-of-plane coupling terms (**B**) are zero. This is a consequence of equal and opposite moments being produced in each half of the laminate cancelling each other out. The laminate is assumed to have free longitudinal boundaries i.e. $N_y = 0$. Hence, Equation (1) reduces to;

$$\begin{Bmatrix} N_x \\ 0 \\ 0 \\ 0 \\ 0 \\ 0 \end{Bmatrix}_L = \begin{bmatrix} A_{11} & A_{12} & 0 & 0 & 0 & 0 \\ A_{21} & A_{22} & 0 & 0 & 0 & 0 \\ 0 & 0 & A_{33} & 0 & 0 & 0 \\ 0 & 0 & 0 & D_{11} & D_{12} & D_{13} \\ 0 & 0 & 0 & D_{21} & D_{22} & D_{23} \\ 0 & 0 & 0 & D_{32} & D_{32} & D_{33} \end{bmatrix}_L \begin{Bmatrix} \varepsilon_x \\ \varepsilon_y \\ 0 \\ 0 \\ 0 \\ 0 \end{Bmatrix}_L \quad \ldots (2)$$

ε_y in row 2 of Equation (2) is non-zero as a consequence of the laminate transverse Poisson's ratio derived from the uniaxial strain ε_x applied to the full laminate. Note here that ε_y can be defined by the laminate Poisson's ratio ν_L i.e.

$$\varepsilon_{y_L} = -\left(\frac{A_{21}}{A_{22}}\right)_L \varepsilon_{x_L} = -\nu_L \varepsilon_{x_L} \quad \ldots (3)$$

Compatibility of strain across the laminate/sublaminate boundary is then applied. The $(\pm\theta)$ sublaminate is balanced but is non-symmetric resulting in the following form of sublaminate constitutive equations;

$$\begin{Bmatrix} N_x \\ N_y \\ N_{xy} \\ M_x \\ M_y \\ M_{xy} \end{Bmatrix}_{\pm\theta} = \begin{bmatrix} A_{11} & A_{12} & 0 & 0 & 0 & B_{13} \\ A_{21} & A_{22} & 0 & 0 & 0 & B_{23} \\ 0 & 0 & A_{33} & B_{13} & B_{23} & 0 \\ 0 & 0 & B_{13} & D_{11} & D_{12} & 0 \\ 0 & 0 & B_{23} & D_{21} & D_{22} & 0 \\ B_{13} & B_{23} & 0 & 0 & 0 & D_{33} \end{bmatrix}_{\pm\theta} \begin{Bmatrix} \varepsilon_x \\ -\nu_L \varepsilon_x \\ 0 \\ 0 \\ 0 \\ 0 \end{Bmatrix}_L \quad \ldots (4)$$

Note that the form of the stiffness matrices in Equation (4) ensures that only N_x, N_y and M_{xy} are non-zero in the load moment vector and that the $\kappa_{xy} = 0$ condition enforced by the flat laminate means a twisting moment M_{xy} is applied to the sublaminate. Consequently, the sublaminate Poisson's ratio can be defined as;

$$\nu_{\pm\theta} = -\left(\frac{A_{21}}{A_{22}}\right)_{\pm\theta} \quad \ldots (5)$$

https://doi.org/10.1017/S000192400000765X Published online by Cambridge University Press

The loads resulting from Equation (4) are input into VICONOPT where a transcendental eigenvalue problem is solved to produce buckling modes and values of sublaminate buckling strain, the lowest of which is taken as the critical sublaminate buckling strain ε^C.

The second stage of the Strip Model is the calculation of the propagation strain ε_{th}. An equivalent Mode I approximation of the actual, mixed-mode Strain Energy Release Rate (SERR) is established by assuming simplified components of bending and membrane (strain) energy in the post-buckled, thin sub-laminate created by the delamination[5]. A comparison of bending and membrane energies in the sublaminate prior to and following propagation results in the following equation for the SERR,

$$G_1 = \frac{A_{nn}}{2}\left(\varepsilon_x - \varepsilon^C\right)\left(\varepsilon_x + 3\varepsilon^C\right) \quad \ldots (6)$$

Here A_{nn} is the axial stiffness of the sub-laminate with $n = 1$ when $A_{11} > A_{22}$ or $n = 2$ when $A_{22} > A_{11}$. By determining when G_I is equal to G_{IC}, the SERR required to cause Mode I failure of the resin, it is possible to approximately predict the threshold strain ε_{th}, below which propagation of a delamination will not occur resulting in the equation,

$$\varepsilon_{th} = \varepsilon^C\left(\sqrt{4 + \frac{2G_{1C}}{A_{nn}(\varepsilon^C)^2}} - 1\right) \quad \ldots (7)$$

Note that, if the laminate/sublaminate boundary is considered, the interaction of the axially compressed sublaminate with the laminate along its boundary can induce additional transverse compression or tension in the sublaminate. This is because $v_{\pm\theta}$ will generally differ from v_L[20]. This is explored in the following.

2.2 Finite Element analysis

An approach to calculating delamination propagation strains for laminates restrained against global laminate buckling by an anti-buckling guide using the nonlinear Finite Element program ABAQUS[21] is briefly described here. A full description of both the Finite Element and Strip Model analyses, including all material modelling data for T700GC/M21, has been published previously[5]. ABAQUS linear eigenvalue solver is used to calculate sublaminate buckling strains. It is also used to provide buckling mode shapes for use as imperfections to determine post-buckling behaviour using non-linear ABAQUS. However, in some cases as an alternative to mode shapes derived from the linear eigenvalue analysis, point loads and analytically derived mode shapes approximating those encountered in the experiments were used to provide imperfections for the non-linear analysis. In the propagation FEA, three parts were used to the model the laminates, with the interface zone, which is populated with cohesive elements, being inserted between the thin sub-laminate and the thick base laminate. Four-noded shell elements (S4) were used in the sub-laminate and base to account for any through-thickness shear deformation that may arise. In order to predict delamination propagation, the zero thickness, eight-noded cohesive elements were employed in conjunction with an energy-based Benzeggagh-Kenane law[22]. FEA results for ε_{th} are based on the strain at which a node first fails i.e. propagation of the delamination[5].

Residual strains induced by cool down from the laminate curing temperature were also considered for some laminates.

https://doi.org/10.1017/S000192400000765X Published online by Cambridge University Press

3.0 EXPERIMENTAL SET-UP

A number of artificially delaminated laminates with (±θ) sublaminates were subject to axial compression at room temperature, see Table 1. (Additional results for artificially delaminated layups with two and three ply thick sublaminates employing 0°, ±45° and 90° ply angles can be found elsewhere[5,23]).

Laminates were manufactured from 0·25mm thick Hexcel T700GC/M21 pre-preg Carbon Fibre Reinforced Plastic (CFRP) layers with material properties E_{11} = 136GPa, E_{22} = 8·9GPa, G_{12} = 4·5GPa, ν_{12} = 0·35 and G_{IC} = 550J/m^2. In order to produce an artificial delamination in each laminate, a single non-stick circle of polytetrafluoro-ethylene (PTFE) 0·0125mm thick and 39mm in diameter was introduced during manufacture. In each case the delamination was placed, on one side only, at the second ply interface. This size of delamination is representative of the upper limits of BVID diameter in an aerospace laminate of this thickness. It was also chosen, based on preliminary analytical studies, to ensure that delamination propagation occurred well within the load capacity of the test machine (Instron 5585H). Laminates will be referred to using the appropriate sublaminate stacking sequence (±θ) except in the case of the non-symmetric laminate with a ±30° sublaminate. This laminate will be referred to as $(\pm 30)_{NS}$. Assuming the laminate is subject to uniaxial compression and remains flat, the sublaminate is only coupled to the laminate via the transverse load placed on it by Poisson's ratio deformation of the laminate, see Equation (4). Hence, laminates (±30), $(\pm 30)_{NS}$, (±45), (±60) and (90_2) were chosen to investigate differences in Poisson's ratio between the laminate and sublaminate while retaining reasonable resistance to compressive loads.

Table 1
Experimental and analytical sublaminate buckling strains and threshold propagation strains for laminates with a range of laminate and sublaminate Poisson's ratios. Results in brackets indicate strain at which sublaminate mode shapes jump. In all cases an artificial delamination of diameter 39mm was placed at the 2nd ply interface and sublaminates thereby created are marked in bold in column 1

Stacking sequence	ν_L	$\nu_{\pm\theta}$	$\nu_{\pm\theta}$ - ν_L	ε^c (μstrain)			ε_{th} (μstrain)		
				Exp.	Strip Model	FEA	Exp.	Strip Model	FEA
[**0$_2$**/±45/90/±45/90]$_S$	0·32	0·35	0·03	1,250*	676	619	3,540	3,552	3,583
[**±30**/0/90$_2$/0/90/0]$_S$	0·15	1·43	1·28	>1,000 (1,460)	444	386	3,600	4,804	4,895
[**±30**/0$_2$/±30/30/∓60/±30/30/0$_2$/∓30]	0·85	1·43	0·58	>1,700 (2,000)	622	471	4,150	4,698	5,535
[**±45**/0$_2$/-45/90/+45/90]$_S$	0·32	0·79	0·47	3,010*	793	687	6,700	6,567	7,350
[**±60**/0$_2$/±30/∓30]$_S$	0·64	0·32	-0·32	-	>10,000	-	-	>10,000	-
[**90$_2$**/±45/0/∓45/0]s	0·32	0·02	-0·30	-	7,092	-	-	7,647	-

*Delayed experimental buckling due to adhesion.

https://doi.org/10.1017/S000192400000765X Published online by Cambridge University Press

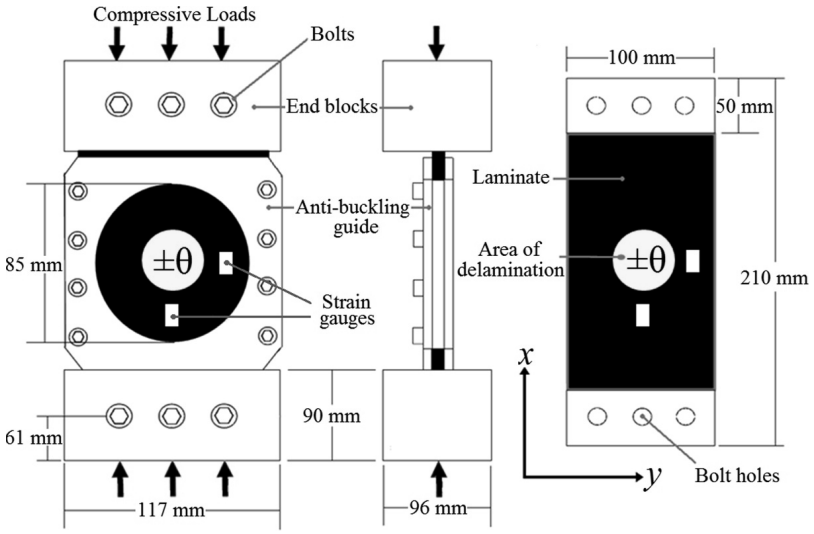

Figure 1(a). Compression fixture with anti-buckling guide and (b) dimensions of coupon with 39mm diameter circular delamination. Strain gauge positions are shown as white rectangles and are orientated vertically.

Mismatches in Poisson's ratio for individual laminate/sublaminate combinations are given in Table 1. Laminates (0_2) and (±45) have been presented previously[5] but are included here to provide a broad range of (±θ) sublaminates and Poisson's ratio mismatches for comparison.

During the axial compression tests, laminates were fitted into a compression rig. The rig consists of two end fixtures producing fully clamped conditions and a circular anti-buckling guide of internal diameter 85mm, see Fig. 1. The anti-buckling guide prevents formation of full laminate buckling modes and resists interaction of laminate and sublaminate buckling[18], yet has a wide enough window to ensure delamination growth can occur unhindered.

Prior to compression, laminates (±30) and $(\pm 30)_{NS}$ were loaded until sublaminate buckling occurred to ensure no adhesion remained between the PTFE and the laminate. Laminates (±60) and (90_2) were also pre-loaded to a reasonable level of load but failed to display sublaminate buckling. During the experiments, axial compression was applied in the x-direction (see Fig. 1) under displacement control at 0·1mm/min until local delamination propagation occurred or, in cases where local buckling did not occur, until laminates suffered global failure. Buckling modes and failure sequences were monitored using a Digital Image Correlation (DIC) system which employs a pair of stereo cameras to measure 3D surface displacement.

To ensure specimens were correctly aligned and placed under pure axial compression, strains were recorded throughout the tests by two pairs of vertically aligned back-to-back strain gauges, see Fig. 1.

4.0 RESULTS

VICONOPT critical buckling strains ε^C for (±θ) sublaminates are plotted on the left hand axis of Fig. 2 for a range of laminate Poisson's ratios, ν_L. The axial A_{11} and transverse A_{22} stiffnesses of a (±θ) sublaminate are plotted against the right-hand axis of Fig. 2. Kinks seen in the ε^C

https://doi.org/10.1017/S000192400000765X Published online by Cambridge University Press

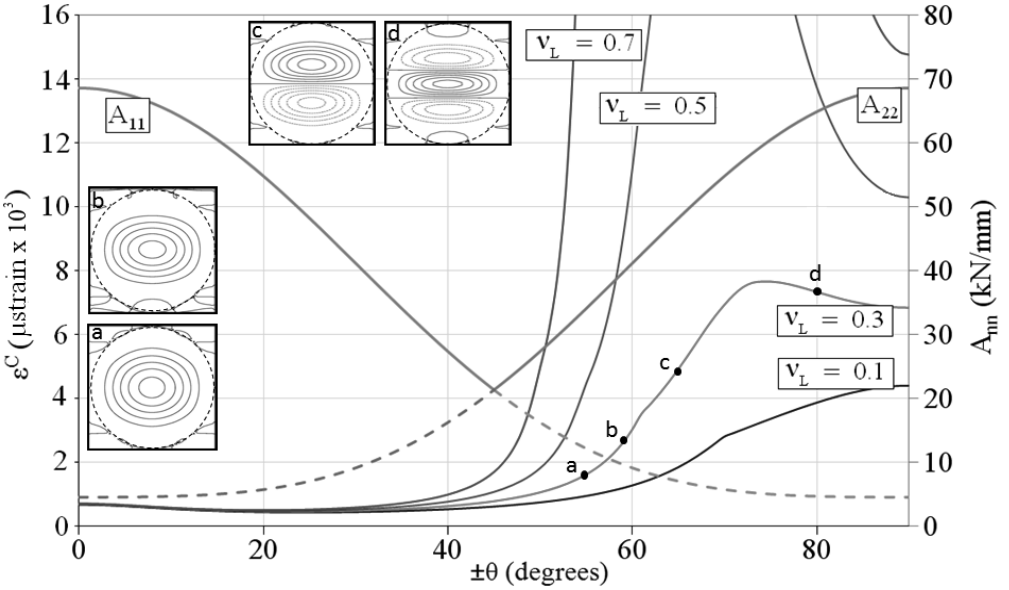

Figure 2. VICONOPT predictions of sublaminate buckling strain at four values of laminate Poisson's ratio ν_L. Overlaid are A_{11} and A_{22} values for ±θ° sublaminates with dashed lines indicating when the A_{nn} value is not used in Equations (6) and (7). Inset are contour plots of VICONOPT buckling modes corresponding to points a, b, c and d where axial load is applied vertically.

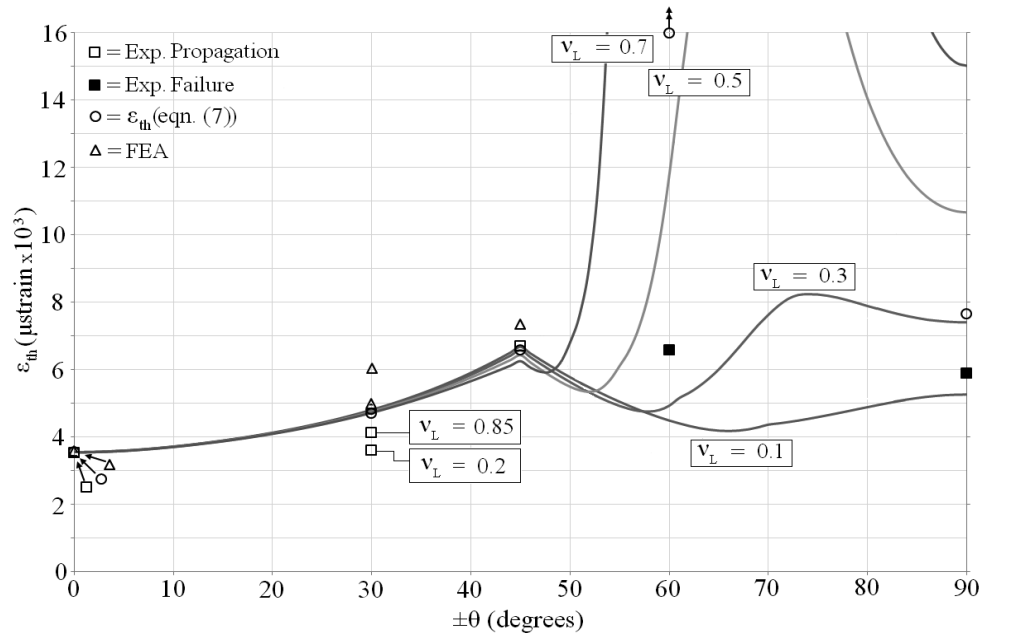

Figure 3. Strip Model delamination propagation ε_{th} (Equation (7)) results (solid lines) for all ±θ° sublaminates at four values of laminate Poisson's ratio ν_L. Experimental, Strip Model and FEA results are represented by squares, circles and triangles, respectively. Squares are open when failure occurred via delamination propagation (following sublaminate buckling) and closed for other modes of failure.

https://doi.org/10.1017/S000192400000765X Published online by Cambridge University Press

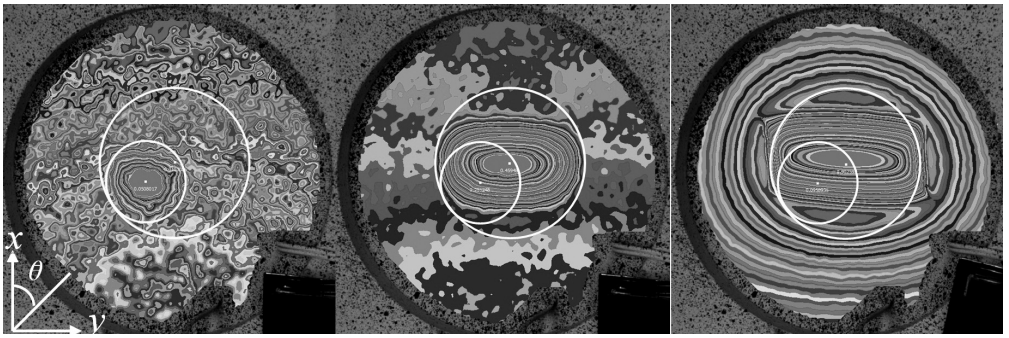

Figure 4. DIC images of (±30) laminate showing (a) fully developed initial asymmetric local buckle (1,450 μstrain), (b) symmetric local buckle following snap (1,460 μstrain) and (c) propagated state with significant sublaminate/laminate buckling interaction (5,410 μstrain). Ply angle θ is shown in (a). The outer white circle indicates the extent of the artificial delamination. The inner white circle indicates the extent of the initial asymmetric sublaminate buckle.

curves in Fig. 2 such as those between points **b** – **c** and **c** – **d** are a consequence of the change in the number of half-waves in the mode shape predicted by VICONOPT as shown in the insets. Analytical results for ε_{th} of a (±θ) sublaminate together with comparative experimental results can be found in Fig. 3. Precise analytical values for ε^C and ε_{th} from the Strip Model and FEA for the experimental coupon tests are given in Table 1. Note that as per Section 2, $(\pm 30)_{NS}$ was assumed to be symmetric i.e. ε_{xy_L} is assumed to be zero in Equations (2) and (4) despite $(\pm 30)_{NS}$ having a small amount of extension-shear coupling A_{13} and A_{23}.

Experimental sublaminate buckling and threshold strain results can also be found in Table 1. The reported experimental strains are an average based on the four strain gauges correlated with buckling and propagation events observed using the DIC system. Sublaminate buckling is detected via a local increase in the number of contours (indicating a steep gradient) on the DIC images (see Fig. 4(a)).

For the (±30) and $(\pm 30)_{NS}$ laminates the point at which sublaminate deformation becomes sublaminate buckling is difficult to determine precisely and hence a lower bound on experimental strains is recorded in Table 1. Due to adhesion between the sublaminate and base laminate, as noted in Table 1, the experimental buckling strain for the (0_2) and (±45) sublaminates was poorly predicted by both VICONOPT and FEA. However, numerous results for sublaminates made up of 0°, ±45° and 90° plies where residual adhesion was removed by pre-loading have been published previously[5]. In these tests both VICONOPT and FEA give accurate and consistent predictions of experimental sublaminate buckling strains. Hence the authors have confidence in the modelling strategies. Laminate bending/buckling within the anti-buckling guide window (see outer circular contours Fig. 4(c)) is similarly detected by an increase in the number of contours.

A snap buckling event, where a sudden jump from a localised asymmetric sublaminate buckling mode shape to an interaction of a symmetric sublaminate buckling mode shape with an overall deformation of the laminate was detected in the (±30) and $(\pm 30)_{NS}$ coupons. The jump occurred suddenly over a single DIC frame, contrast Figs. 4(a) and (b). This sudden jump in sublaminate mode shape has not be seen in previous tests on sublaminates containing 0°, ±45°, and 90° plies[5]. The additional two bracketed results given for the (±30) and $(\pm 30)_{NS}$ laminates in the fifth column of Table 1 give the strain at which the snap or mode jump occurred, see Fig. 4(b).

https://doi.org/10.1017/S000192400000765X Published online by Cambridge University Press

Propagation is deemed to have occurred when the sublaminate buckle spreads outside of the initially delaminated area given by the outer white circle on Fig. 4. The (0_2), (±45) and both (±30) laminates exhibited sublaminate buckling leading to delamination propagation, e.g. see Fig. 4(c). As expected, for all four laminates, delamination propagation occurs in a stable manner i.e. propagation is proportional to the increase in applied strain above ε_{th}. This is a consequence of the sublaminate being relatively thin in comparison to the laminate and can be inferred from Equation (6)[24]. Delaminations placed at deeper interfaces within the laminate tend to produce unstable propagation[10,25] and hence fail more catastrophically. This should be considered when assessing the severity of individual delaminations. However, the general trends about the influence of fibre angle on sublaminate buckling and delamination propagation presented here will apply for other sublaminate thicknesses.

The (±60) laminate did not display any sublaminate buckling; instead a symmetric delamination failure about the core of central plies, independent of the artificial delamination, was detected. It is believed that failure was a result of edge effects induced by large differences in effective Poisson's ratio between ±30° plies and 0° plies[26]. The (90_2) laminate did not display any sublaminate buckling but instead failed near the top clamped edge following buckling of the laminate within the anti-buckling window. This was a result of moments induced in the region of the coupon between the end fixture and the top of the anti-buckling guide, see Fig. 1. Hence, a boundary failure unrelated to the artificial delamination can be considered to have occurred.

5.0 DISCUSSION

5.1 Tolerance of delamination as a function of θ

Laminates with (±θ) sublaminates subject to compressive uniform end-displacement display a variety of behaviours. These are related to stiffness in the x and y directions, mismatches in Poisson's ratio between the laminate and sublaminate, and bend-twist coupling. The effect of these various behaviours is dependent on θ and varies continuously as θ varies from 0° to 90°. However, different effects dominate delamination propagation behaviour for different ranges of θ.

It can be seen from Fig. 2 that for $0° < \theta < 40°$ axial loading dominates the calculation of ε^C. Hence varying ν_L, which only effects transverse loads (Equation (4)), has almost no effect on ε^C. Figure 2 also indicates that for $0° < \theta < 40°$ buckling strain ε^C is relatively low in comparison to other (±θ) sublaminates. Hence, in this case, the mechanism for causing delamination propagation is present at relatively low levels of applied strain.

A comparison of Figs 2 and 3 indicates that A_{11} dominates the calculation of ε_{th} for $0° < \theta < 45°$. Alternatively, this can be established by considering Equation (7) with small ε^C and large A_{11}. For $45° < \theta < 90°$ the value of ε^C dominates the calculation of ε_{th} when the laminate Poisson's ratio ν_L is large. For lower ν_L i.e. small ε^C it is the transverse stiffness, A_{22}, that dominates. Minimum ε_{th} values can be found at $\theta = 0°$ and 90° i.e. the peak of A_{11} and A_{22} curves (see Fig. 2). This indicates that once buckled, axially or transversely stiff sublaminates will produce strong peeling moments at the crack tip leading to low delamination propagation strains. This is demonstrated by results for the (0_2) laminate in Table 1. Note that although the (0_2) sublaminate buckled later than predicted owing to residual adhesion, once buckled the sublaminate carries the expected energy. Hence the Strip Model can correctly predict ε_{th}, see Table 1 and Fig. 3.

https://doi.org/10.1017/S000192400000765X Published online by Cambridge University Press

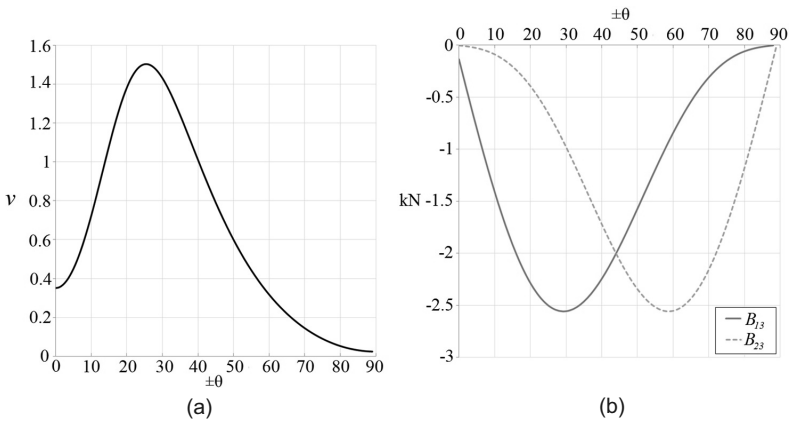

Figure 5. Variation of (a) sublaminate Poisson's ratio $\nu_{\pm\theta}$ and (b) extension-twist coupling stiffnesses B_{13} and B_{23} for a pair of ±θ plies.

Figure 5(a) plots the Poisson's ratio, $\nu_{\pm\theta}$, of the (±θ) sublaminates calculated using T700GC/M21 material properties in Equation (5). It is clear from Fig. 5(a) that sublaminates with $10° < \theta < 40°$ have a relatively high $\nu_{\pm\theta}$. Laminates with large mismatches between $\nu_{\pm\theta}$ and ν_L (see Table 1), with $\nu_{\pm\theta} > \nu_L$, can cause considerable additional transverse compression strains to be applied to the sublaminate[20]. This is a result of the in-plane constraint of the sublaminate boundary by its attachment to the laminate. In the delamination propagation phase the induced transverse compression gives rise to additional inter-ply stresses. From Equation (4) the twisting moment, $M_{xy_{\pm\theta}}$, acting on the sublaminate as a result of the restraint of its boundary by the laminate is given by;

$$M_{xy_{\pm\theta}} = B_{13_{\pm\theta}}\varepsilon_{x_L} - B_{23_{\pm\theta}}\nu_L\varepsilon_{x_L} \quad \ldots (8)$$

Clearly, for $\nu_L < 1$, $M_{xy_{\pm\theta}}$ is maximum when B_{13} is maximum i.e. approximately 30°, see Fig. 5(b). Hence sublaminates with θ close to 30°, e.g. $20° < \theta < 40°$, are likely to be subject to considerable twisting moments which may influence the formation of sublaminate buckling mode shapes and hence effect delamination propagation. This is discussed in section 5.2.

The use of 0° – 40° plies on the surface of a laminate should be avoided where possible, particularly in cases where $\nu_{\pm\theta} - \nu_L$ is large. Although this is easily accomplished in conventional laminate stacking sequence selection where ply angle variation across interfaces can be easily controlled, it may become a problem for tow steered laminates which have a variable range of near surface ±θ° pairs.

Ply angles with $30° < \theta < 40°$ mark the transition between surface plies offering poor damage tolerance characteristics to those with good damage tolerance characteristics. Figure 2 shows that ε^C is higher for $40° < \theta < 60°$ than for $0° < \theta < 40°$. Hence the formation of the delamination propagation mechanism is delayed improving damage tolerance. Equation (5) indicates that twisting moments should typically be lower for $40° < \theta < 60°$ than for $0° < \theta < 40°$ and will reduce considerably as θ tends to 60°, see Fig 5(b). Figure 3 shows that ε_{th} peaks for $40° < \theta < 60°$ for low values of ν_L. This is a consequence of A_{nn} reaching a minimum at 45°. As θ approaches 60°, Equation (7) begins to be dominated by ε^C particularly for high values of ν_L which as noted produce large transverse tensile strains restraining sublaminate buckling, see Fig. 2.

https://doi.org/10.1017/S000192400000765X Published online by Cambridge University Press

ESDU sheet 80023[27] provides equations and data for calculation of the buckling load of a simply-supported square composite plate, placed under uniaxial compression. These equations were used to study the buckling load of a laminate with ±θ° surface sublaminates affixed symmetrically to a generic, low stiffness, isotropic core. Results indicate that 40° < θ < 60° offer the best laminate buckling performance.

As θ increases from 40° to 60° a change in failure mode from buckling driven delamination propagation to other failure modes occurs. For 60° < θ < 90° typically $\nu_L > \nu_{\pm\theta}$ and transverse tension is induced in the sublaminate which acts to delay or entirely prevent sublaminate buckling. As shown on the right hand side of Fig. 2, as the ratio of ν_L to $\nu_{\pm\theta}$ increases, ε^C tends to infinity. This implies ε^C terms dominate Equations (6) and (7). In particular, as can be seen from Figs. 2 and 3, the significant mismatch in the low $\nu_{\pm\theta}$ and high ν_L for the (±60) laminate means the θ predicts an ε^C which far exceeds the experimental failure strain for this laminate (see Table 1 and Fig. 3). This clearly demonstrates that the laminate will not fail as a result of local buckling-driven delamination propagation. This was borne out in the (±60°) experiment.

5.2 (±30) and $(\pm 30)_{NS}$ laminates

As seen in Figs. 4(a) and 6(a), an initial asymmetric sublaminate buckle occurred in (±30) and $(\pm 30)_{NS}$ laminates at strains significantly higher than those predicted by VICONOPT and FEA, see Table 1. Attempts were made to force the occurrence of the initial asymmetric buckle seen in the (±30) laminates in the non-linear FEA using point loads and an asymmetric amplitude perturbation approximating that seen in the initial asymmetric sublaminate buckle. However, ABAQUS was unable to capture the asymmetric mode shape. Thermal effects due to cool down from the cure temperature were also considered in both FEA and VICONOPT. However, predictions for ε^C of the (±30) laminate only increased to 410 μstrain and 554 μstrain for FEA and VICONOPT respectively from the values for ε^C in Table 1.

If higher buckling modes are considered in VICONOPT it is possible to find an asymmetric mode shape (see Fig. 6(b)) partially resembling that seen in both the (±30) and $(\pm 30)_{NS}$ laminates. It is proposed that contact with the base laminate prevents the formation of two of

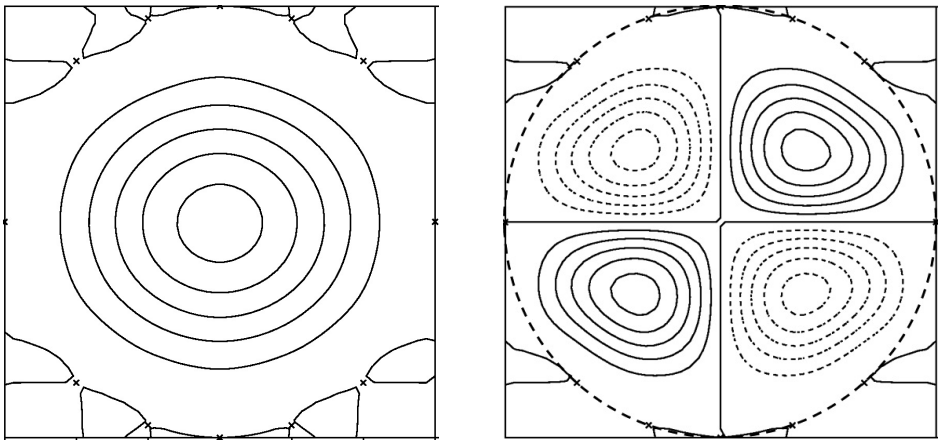

(a) (b)

Figure 6. Contour plot of VICONOPT buckling mode shapes for (±30) sublaminate of (a) the 1st symmetric mode shape associated with the lowest VICONOPT eigenvalue (444 μstrain) and (b) the 5th eigenvalue asymmetric buckling mode shape (1267 μstrain). Load is applied vertically.

https://doi.org/10.1017/S000192400000765X Published online by Cambridge University Press

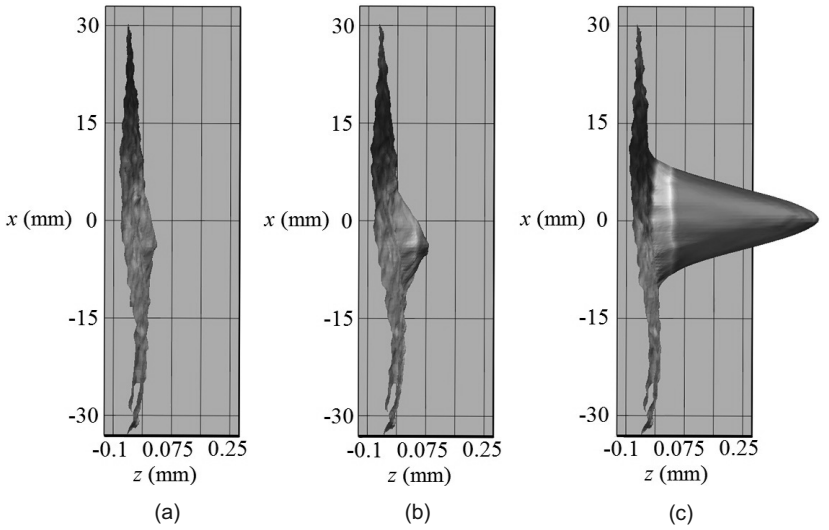

Figure 7. Side view of DIC images for (±30) laminate. (a) Initial formation of asymmetric sublaminate buckling mode and (b) immediately prior to and (c) immediately after jump in sublaminate buckling mode.

the four areas of out-of-plane deformation, contrast Figs. 2(a) and 6(b). Interaction with the overall laminate imperfection (see Fig. 7(a)), is thought to prevent the 3rd area of deformation. The position of the experimental asymmetric mode shape places it in a region of the laminate which is in relative tension which may prevent formation of a symmetric mode shape. Values of ε^C for the asymmetric modes better match those seen experimentally being 1,267 μstrain and 1,759 μstrain for the (±30) and $(\pm 30)_{NS}$ laminates respectively.

The asymmetric nature of the buckling mode shape combined with the strong extension twist coupling effects present in the (±30) and $(\pm 30)_{NS}$ (see Fig. 5(b) and Equation (8)) sublaminates lead the authors to propose that formation of the initial higher energy buckling mode shape seen in (±30) and $(\pm 30)_{NS}$ laminates (Fig. 4(a)) occurs as a consequence of symmetry breaking. It is believed the asymmetric mode is driven by an incompatibility of symmetries between the induced asymmetric twisting forces interacting with an overall asymmetric laminate imperfection (Fig. 8(a)) and the lower energy symmetric sublaminate mode shape e.g. Fig. 6(a). However, if the ε^C from VICONOPT linked to the asymmetric mode shape (Fig. 6(b)) is applied in Equation (6) the predicted ε_{th} (4,493 μstrain and 4,496 μstrain for the (±30) and $(\pm 30)_{NS}$ laminates respectively) indicates that the buckling mode shape may have little effect on the propagation of delaminations in these cases.

The inclusion of a region of increased relative compression on the laminate surface below the sublaminate buckle (see Fig. 7 (b) and (c)) and the symmetric shape of the second sublaminate buckle, indicates that a sudden jump has been made from an unstable twist-driven post-buckling equilibrium path to a stable symmetric post-buckling equilibrium path.

The lateral elongation of the blister indicates that overall laminate bending plays a significant role in this symmetric buckling mode shape. Note that, owing to the unbalanced stacking sequence used in the $(\pm 30)_{NS}$, unlike the post-snap mode shape for the (±30) laminate (see Fig. 2(b)) the symmetric mode shape following snap buckling was rotated by 5° degrees from the horizontal. It is also noted that B_{23} related twisting moments are driven by strains derived from Poisson's ratio mismatches via the induced transverse compression.

https://doi.org/10.1017/S000192400000765X Published online by Cambridge University Press

These effects are especially acute in the post-buckling phase of the (±30) and $(\pm 30)_{NS}$ experiments where $v_{\pm\theta}$ is additionally affected by the curvature caused by the interaction of the sublaminate buckle with deformation of the laminate (see Fig. 2(c)). An analysis of Table 1 shows that FEA correctly predicts that propagation will occur for the (±30) at a lower applied strain than for the $(\pm 30)_{NS}$ laminate. This is not predicted by the Strip Model which is unable to capture the additional compressive strains applied to the sublaminate induced by the interaction of sublaminate and laminate buckling mode shapes.

The bending/buckling of the (±30) laminate violates the thin film assumption of the Strip Model and may be the key contributing factor to the over prediction of ε_{th} in Table 1 by both the Strip Model and FEA. Indeed, an analysis of the (±30) laminate using ABAQUS where the anti-buckling guide window was reduced from 85mm to 40mm, reducing interaction of sublaminate buckling and laminate deformation/buckling, produced an increase in ε_{th} to 5,990μstrain. This highlights the danger of interaction between laminate and sublaminate buckling modes[18].

6.0 CONCLUSIONS AND FUTURE WORK

Testing and analysis of laminates with artificially delaminated (±θ) surface plies has shown that plies with $0° < \theta < 40°$ should be avoided on the surface of the laminate owing to the low strain at which sublaminate buckling-driven delamination propagation occurs. This is due to the increased load that is drawn into the sublaminate owing to the high axial stiffness of the plies. For $10° < \theta < 40°$, when $v_L < 0{\cdot}7$, the high Poisson's ratio of the sublaminate introduces additional compressive interply stresses that may lead to early delamination propagation. Furthermore, sublaminates such as (±30) which have large values of B_{13} are subject to considerable twisting moments and produce unexpected asymmetric sublaminate buckles. These modes subsequently jumped to the expected symmetric mode. Improvement of the analysis methods is required to capture the asymmetric mode shape and the jump to a symmetric mode shape at higher applied strains. Interaction of laminate and sublaminate buckling modes in the (±30) laminate experiments also contributed significantly to the poor damage tolerance of this laminate.

Owing to their high sublaminate buckling resistance and reasonably low axial and transverse stiffnesses, the most favourable surface plies, both in terms of strength following delamination and buckling capacity of the full laminate, are confirmed to be $40° < \theta < 60°$ peaking at ±45°. Additionally, peak laminate buckling load occurs for ±45° surface plies and decreases by up to 29% for 0° and 90° surface plies (for long panels). This indicates that placing ±45° plies on the laminate surface improves both damage tolerance and buckling resistance.

Poisson's ratio mismatches between the full laminate and sublaminate can also have beneficial effects. Surface plies with $60° < \theta < 90°$ will, in many cases ($v_L > 0{\cdot}3$) ensure transverse tensile stresses are induced in the sublaminate, delaying or even preventing buckling of the delaminated sublaminate and thus delamination propagation. However, care should be exercised as such laminates were shown to fail as a result of a mechanism other than sublaminate buckling driven delamination propagation making strength prediction difficult.

The Strip Model is shown to perform well, and in many cases better than Finite Element Analysis, when compared to experiments. In all cases, Finite Element Analysis produced unconservative predictions of the experimental threshold strains and hence its implementation as a predictive or validation method for compression after impact strength should be undertaken with care. Results for both the Strip Model and FEA are less accurate and unconservative when significant Poisson's ratio, extension-twist coupling or interaction of sublaminate and laminate buckling mode shapes are present.

https://doi.org/10.1017/S000192400000765X Published online by Cambridge University Press

ACKNOWLEDGEMENTS

The authors gratefully acknowledge the support of the EPSRC (Grant number: EP/H025898/1), Airbus and GKN Aerospace.

REFERENCES

1. KIM, B.C., POTTER, K. and WEAVER, P. Continuous tow shearing for manufacturing variable angle tow composites, Compos Part A: Appl Sci Manuf, 2012, (doi:10.1016/j.compositesa.2012.02.024).
2. LIU, W. and BUTLER, R. Buckling Optimization of Variable Angle Tow Panels Using Exact Strip Models, Proceedings of the 53rd AIAA, ASME, ASCE, AHS, and ASC Structures, Structural Dynamics, and Materials Conference, Waikiki, Hawaii, USA, April 2012.
3. WU, Z., WEAVER, P.M., RAJU, G. and KIM, B.C. Buckling analysis and optimisation of variable angle tow composites, *Thin wall structures*, 2012, **60**, pp 163-172.
4. RAJU, G., WU, Z., KIM, B.C. and WEAVER, P.M. Prebuckling and buckling analysis of variable angle tow plates with general boundary conditions, *Composite Structures*, 2012, **94**, pp 2961-2970.
5. BUTLER, R., RHEAD, A.T., LIU, W. and KONTIS, N. Compressive strength of delaminated aerospace composites, *Phil Trans Roy Soc A* 2012, **370**, pp 1759-1779.
6. RICCIO, A., SCARAMUZZINO, F. and PERUGINI, P. Embedded delamination growth in composite panels under compressive load, *Composites: Part B*, 2001, **32**, pp 209-218.
7 SHEN, F., LEE, K.H. and TAY, T.E. Modeling delamination growth in laminated composites, *Comp Sci Tech*, 2001, **61**, pp 1239-1251.
8. FU, H. and ZHANG, Y. On the distribution of delamination in composite structures and compressive strength prediction for laminates with embedded delaminations, *Appl Compos Mater*, 2011, **18**, pp 253–269.
9. TAFRESHI, A. and OSWALD, T. Global buckling behaviour and local damage propagation in composite plates with embedded delaminations, *Int J Pressure Vessels and Piping*, 2003, **80**, pp 9–20.
10. WADEE, M.A. and VÖLLMECKE, C. Semi-analytical modelling of buckling driven delamination in uniaxially compressed damaged plates, *IMA J Applied Mathematics*, 2011, **76**, pp 120−145.
11. CRAVEN, R., IANNUCCI, L. and OLSSON, R. Delamination buckling: A finite element study with realistic delamination shapes, multiple delaminations and fibre fracture cracks, Composites: Part A, 2010, **41**, pp 684–692.
12. SUEMASU, H., IRIE, T. and ISHIKAWA, T. Buckling and post-buckling behavior of composite plates containing multiple delaminations, *J Comp Mats*, 2009, **43**, (02), pp 191-202.
13. ZHANG, Y. and WANG, S. Buckling, post-buckling and delamination propagation in debonded composite laminates Part 1: Theoretical development, *Composite Structures*, 2009, 88, pp 121–130.
14. RHEAD, A.T. and BUTLER, R. Compressive static strength model for impact damaged laminates, *Compos Sci Technol*, 2009, **69**, (14), pp 2301-2307.
15. CHAI, H., BABCOCK, C.D. and KNAUSS, W.G. One dimensional modelling of failure in laminated plates by delamination buckling, *Int J Structures*, 1981, **17**, (11), pp 1069-1083.
16. HUTCHINSON, J.W. and SUO, Z. Mixed mode cracking in layered materials, *Adv Appl Mech*, 1992, **29**, pp 63-191.
17. WILLIAMS, J.G. On the calculation of energy release rates for cracked laminates, *Int J Frac*, 1992, **36**, pp 101-119.
18. RHEAD, A.T., BUTLER, R. and HUNT, G.W. Compressive Strength Following Delamination Induced Interaction of Panel and Sublaminate Buckling, Proceedings of the 53rd AIAA, ASME, ASCE, AHS, and ASC Structures, Structural Dynamics, and Materials Conference, Waikiki, Hawaii, USA, April 2012.
19. WILLIAMS, F.W., KENNEDY, D., BUTLER, R. and ANDERSON, M.S. VICONOPT: program for exact vibration and buckling analysis or design of prismatic plate assemblies, *AIAA J*, 1991, **29**, pp 1927–1928.
20. SHIVAKUMAR, K.N. and WHITCOMBE J.D. Buckling of a sublaminate in a quasi-isotropic composite laminate, *J Compos Maters*, 1985, **19**, (1), pp 2-18.
21. ABAQUS, ABAQUS Analysis User's Manual 2009, Version 6.9. Dassault Systèmes Simulia Corp, Providence, RI, USA 2009.

22. BENZEGGAGH, M. L. and KENANE, M. Measurement of mixed-mode delamination fracture toughness of unidirectional glass/epoxy composites with mixed-mode bending apparatus, *Comp Sci and Tech*, 1996, **56**, pp 439–449.
23. RHEAD, A.T. and BUTLER, R. Buckling, propagation and stability of delaminated anisotropic layers Proceedings of ECCM 14, Budapest, Hungary, 2010.
24. RHEAD, A.T., BUTLER, R. and HUNT, G.W. Post-buckled propagation model for compressive fatigue of impact damaged laminates, *Int J Solids Struct*, 2008, **45**, (16), pp 4349–61.
25. HUNT, G.W., HU, B., BUTLER, R., ALMOND, D.P. and WRIGHT, J.E. Nonlinear modeling of delaminated struts, *AIAA J*, November 2004, **42**, (11), pp 2364-2372.
26. FENSKE, M.T. and VIZZINI, A.J. The inclusion of in-plane stresses in delamination criteria, *J Comp Mats*, 2001, **35**, (15), pp 1325-1342.
27. ESDU 80023, Buckling of rectangular specially orthotropic plates. www.esdu.com.

https://doi.org/10.1017/S000192400000765X Published online by Cambridge University Press